High-performance colorimetric sensor based on PtRu bimetallic nanozyme for xanthine analysis

Mengjun Wang [a,b,*], Minghang Jiang [a], Xiaojun Luo [a], Liyun Zhang [a], Yi He [a], Fanjie Xue [a], Xingguang Su [b,**]

[a] Department of Chemistry, School of Science, Xihua University, Chengdu, Sichuan 610039, China
[b] Department of Analytical Chemistry, College of Chemistry, Jilin University, Changchun, 130012, China

ARTICLE INFO

ABSTRACT

The identification and quantification of xanthine are crucial for assessing the freshness and quality of food products, particularly in the seafood industry. Herein, a new approach was developed, involving the in-situ controllable growth of $Pt_{91}Ru_9$ nanoparticles on graphitic carbon nitride to yield $Pt_{91}Ru_9@C_3N_4$ catalytic materials. By integrating $Pt_{91}Ru_9@C_3N_4$ with the xanthine/xanthine oxidase (XOD) enzyme catalytic system, a nanozyme-enzyme tandem platform was obtained for the quantification analysis of xanthine. Under the catalytic oxidation of xanthine by XOD in the presence O_2, H_2O_2 was generated. Upon the addition of peroxidase-like activity of $Pt_{91}Ru_9@C_3N_4$, H_2O_2 can be decomposed into $\bullet OH$ and $^1O_2$, which can further catalyze the oxidation of TMB to its oxidation product oxTMB with an absorption peak at 652 nm. This smartphone-assisted portable colorimetric sensor for visual monitoring xanthine with a low detection limit of 8.92 nmol L^{-1}, and successfully applied to detect xanthine in grass carp and serum samples.

1. Introduction

In the food industry, maintaining the freshness of fish meat is paramount for ensuring the production of safe and high-quality products. After the death of fish, adenosine triphosphate (ATP) within their bodies degrades successively into adenosine diphosphate (ADP), adenosine 5′-monophosphate (AMP), inosine 5′-phosphate (IMP), inosine (In), hypoxanthine (HX) and xanthine (Dervisevic et al., 2015) (Fig. S1). The concentration of xanthine increased with the prolonged storage time of fish meat (Tripathi et al., 2022). Monitoring the concentration of xanthine in fish meat is regarded as essential means for assessing its freshness (Xu et al., 2024). Xanthine is a critical intermediate in purine nucleotides and deoxyribonucleotides metabolism, with widespread distribution in the organs and bloodstream of humans and other organisms (Jiang et al., 2024). The abnormal levels of xanthine in the blood and urine are also associated with various diseases, such as hyperuricemia, cerebral ischemia, tumors and renal failure (An et al., 2022; Lu et al., 2020). Thus, the development of sensitive, reliable, and rapid sensors for the monitoring and quantification of xanthine is vital for the clinical diagnosis and industrial production. Several analytic al

strategies have so far been developed for xanthine analysis, including colorimetry, voltammetry, and fluorescence techniques (Jesny & Girish Kumar, 2017; Lu et al., 2020; Wang et al., 2022). Among these, the colorimetric approach is more practical due to its rapid response and simplicity. According to previous studies, integrating nanozyme-mediated colorimetric sensing strategies with bio-enzyme could establish enzyme-nanozyme cascade sensing platforms to yield sensing systems with improved sensitivities and broadened determination range (Li, Xie, et al., 2024; Song et al., 2023).

Nanozymes are nanoscale materials with inherent enzyme-mimicking activity, exhibiting both the structural properties of nanomaterials and catalytic functionalities of bio-enzymes (Qiao et al., 2023; Zou et al., 2023). Despite the existence of numerous excellent materials, the development of nanozymes with the characteristics of high stability and robust catalytic performance of is still the focus and hotspot of current research (Geng et al., 2024). To achieve satisfactory catalytical activities, continual adjustments of structural and morphological characteristics of nanozymes are necessary. Among regulatory strategies, elemental doping can effectively modulate the electronic structure and geometry of nanozymes by introducing specific elements into

---

* Corresponding author at: Department of Chemistry, School of Science, Xihua University, Chengdu, Sichuan 610039, China.
** Corresponding author.
E-mail addresses: mjwang@mail.xhu.edu.cn (M. Wang), suxg@jlu.edu.cn (X. Su).

nanomaterials, thereby regulating the catalytic performance of the nanomaterials (Guan et al., 2023; Song et al., 2022). For instance, nanozymes containing metal Pt and Ru as active centers exhibit robust catalytic properties with widespread application in analytical sensing (Liu et al., 2020; Wang et al., 2023). For example, Li et al. (2023) successfully prepared Au–Pt nanoclusters with robust catalytic performance for use as an efficient catalytic label in the development of a colorimetric sensing platform for the highly sensitive analysis of D-dimer. Park et al. (2021) synthesized PVP-stabilized Pt/Ru nanozymes with synergistic enhancement effects for dual-mode colorimetric and fluorescent analysis of glucose in artificial urine and serum samples. Accordingly, the design and development of nanozymes with robust peroxidase-mimic activities for the construction of enzyme-nanozyme cascade colorimetric sensing platforms could achieve sensitive and rapid analysis of xanthine.

Herein, a new approach was developed, involving the in-situ controllable growth of $Pt_{91}Ru_9$ nanoparticles on graphitic carbon nitride to yield $Pt_{91}Ru_9@C_3N_4$. The resulting $Pt_{91}Ru_9@C_3N_4$ exhibited robust peroxidase-mimic activity with a satisfactory affinity toward TMB (0.16 mmol L^{-1}), and the synergistic interplay between Pt and Ru effectively promoted the catalytic activity of $Pt_{91}Ru_9@C_3N_4$ at pH 6. The combination of the prepared $Pt_{91}Ru_9@C_3N_4$ with xanthine oxidase (XOD) resulted in a nanozyme-natural nanozyme tandem platform with remarkable sensitivity toward the quantification analysis of xanthine (Scheme 1). With the catalysis of XOD, xanthine was oxidized by O_2 dissolved in the solution to generate H_2O_2 (Fig. S2). H_2O_2 was then decomposed into •OH and $^1O_2$ by Fenton-like reaction using the peroxidase-like activity of $Pt_{91}Ru_9@C_3N_4$. The generated ROS species quickly initiated the chromogenic reaction of 3,3′,5,5′-tetramethylbenzidine (TMB). Changes in absorption signals demonstrated excellent analytical performance of the $Pt_{91}Ru_9@C_3N_4$-based colorimetric sensing platform for xanthine in real urine and serum samples, with a low detection limit of 8.92 nmol L^{-1}. Meanwhile, the recording of RGB values of color changes at various xanthine concentrations established a relationship between xanthine and color characteristic values for on-site and quantitative analysis of xanthine. In sum, the proposed approach for designing efficient bimetallic nanozymes is potential for future construction of enzyme-nanozyme cascade sensing systems for visual analysis of relevant analytes in food and biological systems.

2. Experimental

2.1. Chemicals and apparatus

Ruthenium (III) chloride trihydrate ($RuCl_3 \cdot 3H_2O$), chloroplatinic acid hexahydrate ($H_2PtCl_6 \cdot 6H_2O$), 3,3′,5,5′-tetramethylbenzidine (TMB), and sodium borohydride ($NaBH_4$) were bought from Sigma-Aldrich (Shanghai, China). Melamine, isopropyl alcohol (IPA), p-benzoquinone (p-BQ), sodium azide (NaN_3), sodium acetate (NaAc), acetic acid (HAc), hydrogen peroxide (H_2O_2), and sodium citrate dihydrate (SCD) were purchased from Beijing Chemical Works. Xanthine oxidase (XOD), xanthine, uric acid, and urea were bought from Yuanye Biotechnology Co., Ltd. (Shanghai, China). All individual solutions were prepared with 18 MΩ deionized water.

UV–vis measurements were recorded on a SHIMADZU UV-2700 UV–visible spectrophotometer. The surface element compositions and valence states of $Pt_{91}Ru_9@C_3N_4$ was analyzed using an X-ray photoelectron spectrometer (XPS) (ThermoFischer , ESCALAB Xi+). Field-emission scanning electron microscopy (SEM, FEI Nova Nano-450), transmission electron microscopy (TEM, Talos F200X) and elemental mapping images were utilized for the surface morphology and structural characterizations. Zeta potential of C_3N_4 and $Pt_{91}Ru_9@C_3N_4$ were carried out on a Zeta-sizer (Nano-S90, Malvern, UK). X-ray diffraction (XRD) analysis was achieved on a SmartLab SE (Japan Rigaku Co.).

2.2. Synthesis of C_3N_4 nanosheets

Firstly, bulk C_3N_4 was prepared using a previously reported method (Wang et al., 2020). 20 g of melamine was calcined at 550 °C for 4 h in a tube furnace. After cooling down to 25 °C, a light-yellow C_3N_4 solid was obtained. To prepare C_3N_4 nanosheets, 1 g of bulk C_3N_4 powder was dispersed in 120 mL of 5 mol·L^{-1} HNO_3 and refluxed for 24 h. The resulting product underwent several washes with deionized water until achieving a nearly neutral pH. Finally, the C_3N_4 suspension was sonicated and centrifuged at 8000 rpm for 12 min to remove unexfoliated nanosheets, followed by freeze-drying to obtain monodisperse C_3N_4 nanosheets.

2.3. Synthesis of $Pt_{39}Ru_{61}@C_3N_4(39:61)$, $Pt_{85}Ru_{15}@C_3N_4(85:15)$, $Pt_{91}Ru_9@C_3N_4(91:9)$, and $Pt_{93}Ru_7@C_3N_4(93:7)$

$Pt_xAu_y@C_3N_4$ catalysts with variable Pt/Au mass ratios were prepared through a facile co-reduction process using sodium borohydride
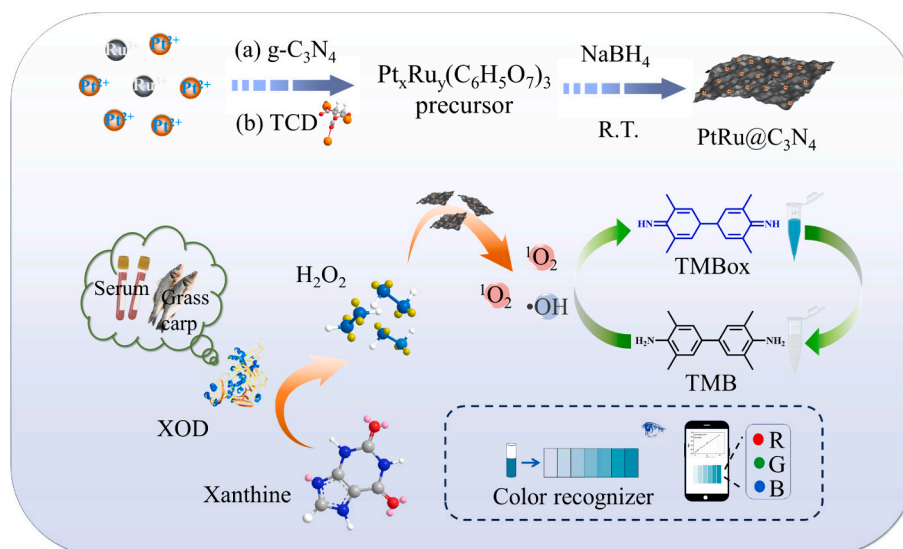
Scheme 1. Illustration of constructing $Pt_{91}Ru_9@C_3N_4$-based biosensor for xanthine assay.

(NaBH$_4$) and sodium citrate tribasic dihydrate (C$_6$H$_5$Na$_3$O$_7$·2H$_2$O) at room temperature. The synthesis process of Pt$_{91}$Ru$_9$@C$_3$N$_4$ consisted of first mixing 0.33 mL of RuCl$_3$·3H$_2$O (38.60 mmol L^{-1}) with 1.67 mL of H$_2$PtCl$_6$·6H$_2$O (38.60 mmol L^{-1}). Subsequently, 16 mL of an aqueous solution containing C$_3$N$_4$ (1.25 mg mL^{-1}) was added to the mixture, and the entire solution was stirred for 10 min. After stirring well, 4 mL of C$_6$H$_5$Na$_3$O$_7$·2H$_2$O (6 mg mL^{-1}) was added dropwise to the suspension, followed by 20 mL of NaBH$_4$ (1.25 mg mL^{-1}), and the co-reduction reaction continued for 12 h (Jiang et al., 2022). The resulting crude product was filtered, washed by alternately ethanol and H$_2$O, and dried at 65 °C for 15 h to obtain the pure product Pt$_{91}$Ru$_9$@C$_3$N$_4$. The synthesis of Pt$_{39}$Ru$_{61}$@C$_3$N$_4$, Pt$_{85}$Ru$_{15}$@C$_3$N$_4$ and Pt$_{93}$Ru$_7$@C$_3$N$_4$ was carried out by the same methodology employed for Pt$_{91}$Ru$_9$@C$_3$N$_4$, with variations in the quantities of added metal precursor solutions. The two control samples, Pt@C$_3$N$_4$ and Ru@C$_3$N$_4$ were prepared by an identical method, omitting the addition of RuCl$_3$·3H$_2$O-water solution and H$_2$PtCl$_6$·6H$_2$O-water solution, respectively.

2.4. Kinetics assays of Pt$_{91}$Ru$_9$@C$_3$N$_4$

The kinetic assays of Pt$_{91}$Ru$_9$@C$_3$N$_4$ were assessed using TMB and H$_2$O$_2$ as substrates. TMB is widely preferred as a chromogenic substrate for both enzyme-catalyzed reactions and nanomaterial catalytic systems due to its high sensitivity, excellent color purity, and the stability of oxidation products (Wu et al., 2019; Zhang et al., 2020). To achieve optimal catalytic performance, various factors including temperature, reaction time, and contents of H$_2$O$_2$ and Pt$_{91}$Ru$_9$@C$_3$N$_4$, were systematically optimized. Under the optimal conditions, the steady-state kinetics of Pt$_{91}$Ru$_9$@C$_3$N$_4$ were conducted in 0.01 mol L^{-1} HAc-NaAc buffer (pH 5) containing 2.5 μg mL^{-1} Pt$_{91}$Ru$_9$@C$_3$N$_4$. For H$_2$O$_2$ concentration maintained at 0.5 mmol L^{-1}, TMB was varied from 0.05 to 0.3 mmol L^{-1} to yield final concentrations of 0.05, 0.075, 0.1, 0.125, 0.175, 0.2, 0.25, and 0.3 mmol L^{-1}. Likewise, H$_2$O$_2$ was adjusted in the range of 0.1–0.8 mmol L^{-1} to yield final concentrations of 0.1, 0.2, 0.3, 0.4, 0.5, 0.6 and 0.8 mmol L^{-1} at a constant TMB concentration of 0.2 mmol L^{-1}.

The UV–vis absorbances at 652 nm were measured 30 s post-reaction. Finally, the K_m and V_{max} values were obtained through double-reciprocal Lineweaver-Burk plots using the following equation (Chai et al., 2023; Yang, Yuan, et al., 2024):

$$\frac{1}{V_0} = \frac{K_m}{V_{max}} \left(\frac{1}{[S]} + \frac{1}{K_m} \right)$$

where V_0 denotes the initial rate, V_{max} is the maximal reaction velocity, [S] refers to the substrate concentration, and K_m denotes the Michaelis constant.

2.5. Xanthine analysis

The process consisted of introducing 200 μL of xanthine concentration (0–300 μmol L^{-1}) and 40 μL XOD (20 U mL^{-1}) into 50 μL phosphate buffer solution (PBS, 0.1 mol L^{-1}, pH 8) at 37 °C. After 25 min of incubation, 50 μL Pt$_{91}$Ru$_9$@C$_3$N$_4$ (0.6 mg mL^{-1}), 300 μL PBS (pH 5, mol L^{-1}) and 200 μL TMB (2 mmol L^{-1}) were introduced, and the mixture was incubated at 45 °C for an additional 10 min. Afterward, 1160 μL H$_2$O were added to the mixture and the absorbance-concentration curves were recorded in the range of 500–800 nm.

2.6. Xanthine analysis with a smartphone

To achieve portable xanthine analysis, the RGB color signal was directly recorded and analyzed by a smartphone application (Chen et al., 2023). The samples to be tested were prepared by the same procedure as described in the xanthine colorimetric assay of Section 2.5, followed by transfer to a 24-well microplate. Under consistent lighting conditions,

the smartphone captured a colorimetric image of the solution, followed by subsequent analysis using ImageJ to obtain the grayscale value.

2.7. Analysis of xanthine in real sample

The practicality of the Pt$_{91}$Ru$_9$@C$_3$N$_4$/TMB/XOD-based colorimetric sensor was validated in grass carp and blood samples. Blood samples were obtained from the Third Bethune Hospital of Jilin University, and the grass carp were purchased from a local seafood market. The serum sample processing method can be found in our previous work (Zhang et al., 2019). The serum samples were filtered using a 0.22 μm filter membrane, followed by centrifugation at 11,000 rpm for 10 min. The supernatant was collected and neutralized with NaOH to a neutral pH. Then, the neutral serum sample was diluted 50-fold with deionized water, and the xanthine solutions were added to achieve the final xanthine concentrations of 0, 20, 60, and 100 μmol L^{-1}. Subsequently, the analysis of xanthine in serum samples was conducted as described in Section 2.5.

The live grass carp were purchased and then euthanized using the electrical stunning method by the skilled seller. Percussive stunning was performed by trained staff to minimize stress reactions. Following euthanasia, the fish were immediately immersed in an ice slurry within a styrofoam box. This box, containing the euthanized fish, was promptly transported to the laboratory and processed under sterile conditions to prepare fish meat samples. In the laboratory, the killed fish was scaled, gutted, decapitated, and rinsed in flowing tap water to remove the blood and viscera (Xu et al., 2024; Zhang et al., 2018). This process strictly adhered to the guidelines recommended by the Directive 2010/63/EU of the European Parliament and of the Council of 22 September 2010 on the protection of animals used for scientific purposes. Subsequently, the fresh fish meat was ground into a homogenate, then the resulting homogenate was combined with ultra-pure water at a ratio of 1:3 (*w/w*). After filtering through a filter paper, the fish homogenate was mixed with varying contents of xanthine to create spiked samples with final concentrations of 0, 20, 60, and 100 μmol L^{-1}. The correlation between the increase in xanthine concentration and the degree of fish spoilage (Dervisevic et al., 2015) prompted us to conduct xanthine analysis on grass carp samples stored at 4 °C for different durations (0, 96, and 168 h). Finally, the analysis of xanthine in serum and grass carp samples was conducted following the above-outlined procedure (Section 2.5).

3. Results and discussions

3.1. Fabrication and characterization of Pt$_{91}$Ru$_9$@C$_3$N$_4$

In this study, PtRu@C$_3$N$_4$ was prepared through the mild co-reduction process shown in Fig. 1a. The experiments revealed a platinum-to-ruthenium mass ratio of 91:9 as optimal to yield exceptional catalytical performance of PtRu nanoparticles, thereby used in subsequent experiments (Fig. S3). As illustrated in Fig. S4, the zeta potential of Pt$_{91}$Ru$_9$@C$_3$N$_4$ was estimated to be −20.75 ± 0.77 mV, a value slightly more positive than that of C$_3$N$_4$ (−21.65 ± 0.35 mV). The notable change in surface charge was probably due to the presence of positively charged metal ions in Pt$_{91}$Ru$_9$@C$_3$N$_4$ (Shen et al., 2023). Pt$_{91}$Ru$_9$@C$_3$N$_4$ with negatively charged surface, exhibits favorable affinity for TMB (Zhou, Chen, et al., 2022), which contains two amine groups, through electrostatic attraction. The robust affinity between the catalyst and its substrate contributes to the improved catalytic efficiency of the catalyst. The microstructure of Pt$_{91}$Ru$_9$@C$_3$N$_4$ was characterized by transmission electron microscopy (TEM). As displayed in Fig. 1b-e, uniformly distributed PtRu nanoparticles with an average size of approximately 4.14 nm were formed on the entire surface of C$_3$N$_4$. The lattice distance of Pt$_{91}$Ru$_9$@C$_3$N$_4$ was determined to be approximately 0.22 nm, implying successfully prepared catalytic material (Li et al., 2023). From Fig. 1f, the Pt/Ru atomic fraction ratio in Pt$_{91}$Ru$_9$@C$_3$N$_4$ estimated by energy dispersive spectroscopy (EDS) to be 4.23:1. The

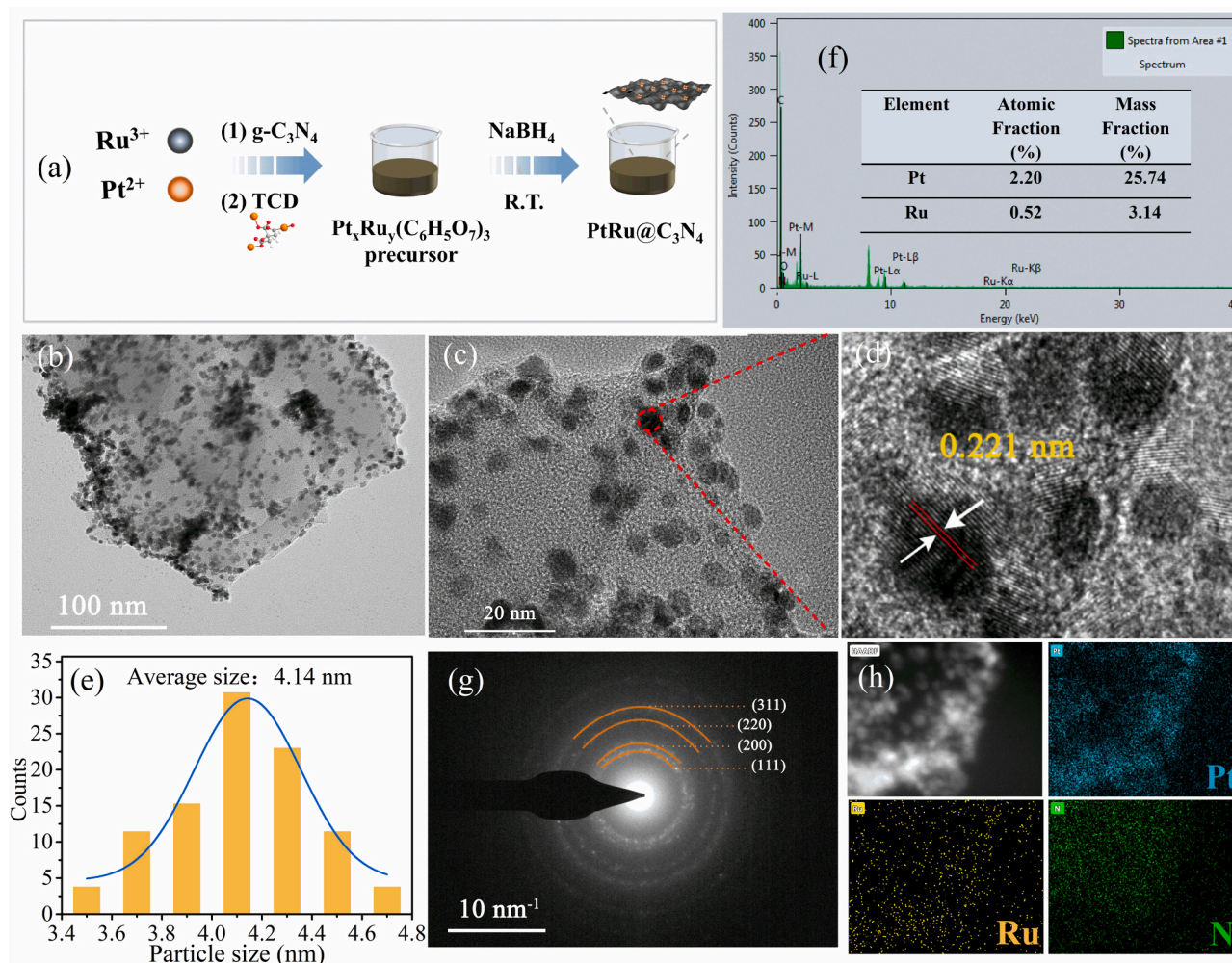**Fig. 1.** (a) Illustration of $Pt_{91}Ru_9@C_3N_4$ synthesis. (b-d) TEM images of $Pt_{91}Ru_9@C_3N_4$. (e) Size distribution of $Pt_{91}Ru_9@C_3N_4$. (f) EDS analysis of $Pt_{91}Ru_9@C_3N_4$. The inset shows the atomic and mass proportions of Pt and Ru. (g) SAED pattern and (h) element mapping of $Pt_{91}Ru_9@C_3N_4$.

selected area electron diffraction (SAED) patterns in Fig. 1g revealed $Pt_{91}Ru_9@C_3N_4$ featuring a face-centered cubic lattice structure with four rings corresponding to (111), (200), (220) and (311) crystal planes (from inner to outer rings). The images captured by EDS mapping in Fig. 1h showed the elements Pt, Ru, and N were uniformly distributed in the $Pt_{91}Ru_9@C_3N_4$ nanozyme, which demonstrated that PtRu was evenly modified on C_3N_4 nanosheets.

The X-ray diffraction (XRD) patterns of various catalysts, including $Pt@C_3N_4$, $Pt_{39}Ru_{61}@C_3N_4$, $Pt_{85}Ru_{15}@C_3N_4$, $Pt_{91}Ru_9@C_3N_4$, $Pt_{93}Ru_7@C_3N_4$, and $Ru@C_3N_4$ are presented in Fig. 2a. The peaks at 2θ values of $39.7°$, $46.3°$, $67.4°$, and $80.3°$ corresponded to the (111), (200), (220) and (311) planes, respectively. No obvious Ru or related oxide diffraction peaks were observed, indicating no phase separation in the $Pt_xRu_y@C_3N_4$. In Fig. 2b, the broad XRD peaks of all samples were observed in the 2θ angle range between $36.5°$ and $48°$. As $RuCl_3 \cdot 3H_2O$ content rose, the diffraction peak of the (111) plane gradually sharpened, suggesting variation in the Pt–Ru ratio within the Pt–Ru alloy nanostructure. Thus, the alloying degree of $PtRu@C_3N_4$ can be effectively controlled by varying the quantity of Pt–Ru metal precursor, consistent with the SAED analysis observed in Fig. 1g.

The elemental composition and valence state of $Pt_{91}Ru_9@C_3N_4$ were explored by X-ray photoelectron spectroscopy (XPS). In Fig. 2c, elements like Pt, Ru, N, and O were presented in the wide-scan XPS of $Pt_{91}Ru_9@C_3N_4$. In Fig. 2d, the Pt 4f segment showed the existence of Pt species in the Pt^0/Pt^{2+} state (Liu et al., 2020). In Fig. 2e, the peaks at

462.04 and 465.09 eV corresponded to Ru^0 and Ru^{4+} species, respectively, based on the spin-orbit splitting of Ru $3p_{3/2}$. The others at 484.48 and 487.14 eV were ascribed to Ru^0 and Ru^{4+} of Ru $3p_{5/2}$, respectively. Besides, $Pt_{91}Ru_9@C_3N_4$ contained Pt/Ru at an atomic ratio of 6.63:1, suggesting a strong alloy effect (Table S1). The N 1 s spectrum in $Pt_{91}Ru_9@C_3N_4$ (Fig. 2f) can be fitted into five nitrogen species, corresponding to pyridinic N (398.47 eV), $M-N_x$ (399.02 eV), pyrrolic N (400.32 eV), graphic N (401.39 eV) and oxidized N (404.51 eV) (Lyu et al., 2024). The presence of $M-N_x$ peaks signified an effective association between metal atoms and N atoms. Such interactions enhanced the stability of metal atoms on the support owing to the superior adsorption ability of pyridine nitrogen in forming coordination bonds with metal atoms (Wang et al., 2021).

3.2. Peroxidase activity of $Pt_{91}Ru_9@C_3N_4$

The peroxidase activity of $Pt_{91}Ru_9@C_3N_4$ was systematically explored. As illustrated in Fig. 3a, the presence of H_2O_2 and $Pt_{91}Ru_9@C_3N_4$ resulted in TMB oxidation to oxTMB to yield a deep blue color. By comparison, no significant absorption peak was observed in the presence of only $Pt_{91}Ru_9@C_3N_4$, C_3N_4, or H_2O_2. The absorbance value at 652 nm with $Pt_{91}Ru_9@C_3N_4$ was higher than those observed with $Pt@C_3N_4$ and $Ru@C_3N_4$ (Fig. 3b), indicating superior catalytic activity of $Pt_{91}Ru_9@C_3N_4$. These features elucidated the presence of a synergistic effect between the metallic Pt and Ru, leading to the superior
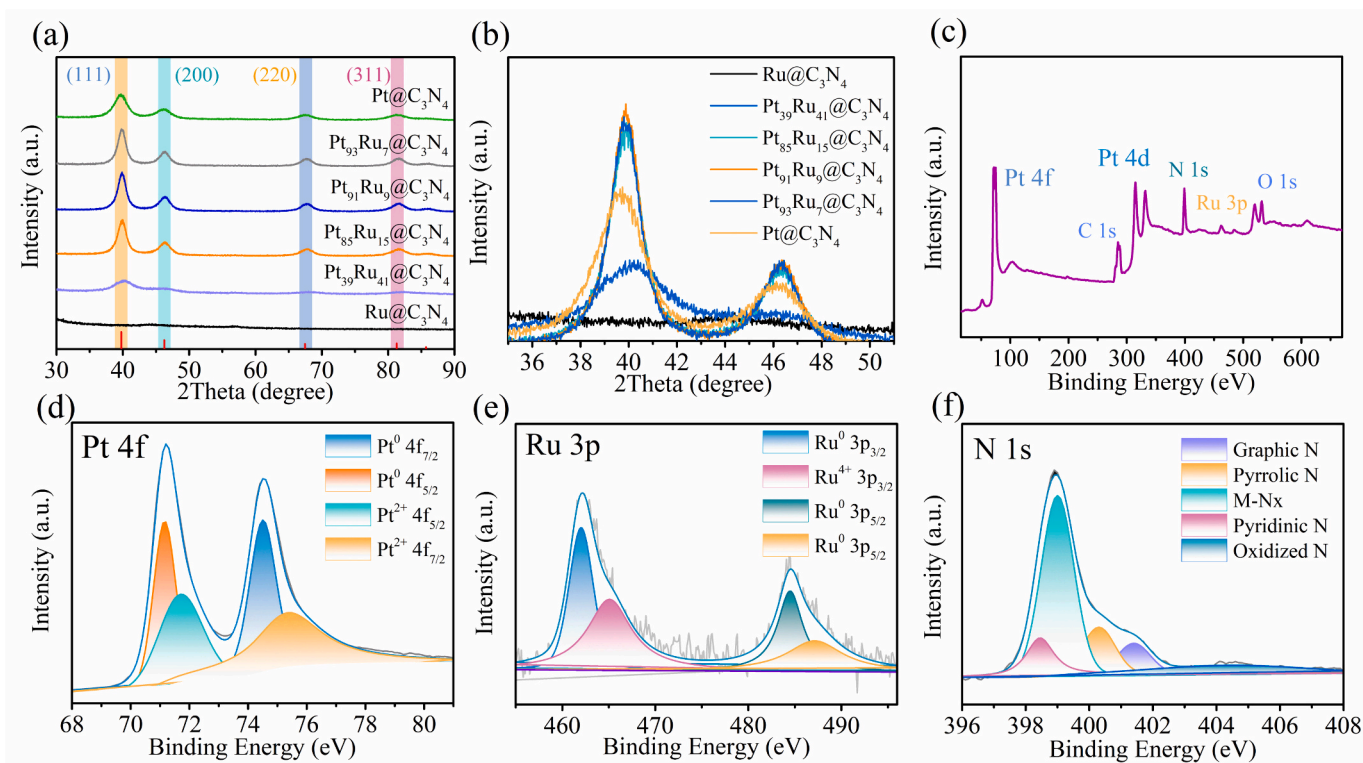
Fig. 2. (a) XRD patterns of the Pt@C$_3$N$_4$, Pt$_{93}$Ru$_7$@C$_3$N$_4$, Pt$_{91}$Ru$_9$@C$_3$N$_4$, Pt$_{85}$Ru$_{15}$@C$_3$N$_4$, Pt$_{39}$Ru$_{61}$@C$_3$N$_4$ catalysts. (b) Magnified XRD profiles of all samples in the 2θ angle range between 36.5 and 48°. (c) XPS spectra of Pt$_{91}$Ru$_9$@C$_3$N$_4$. (d-f) Pt 4f, Ru 3p and N 1 s XPS high-resolution spectra of Pt$_{91}$Ru$_9$@C$_3$N$_4$.
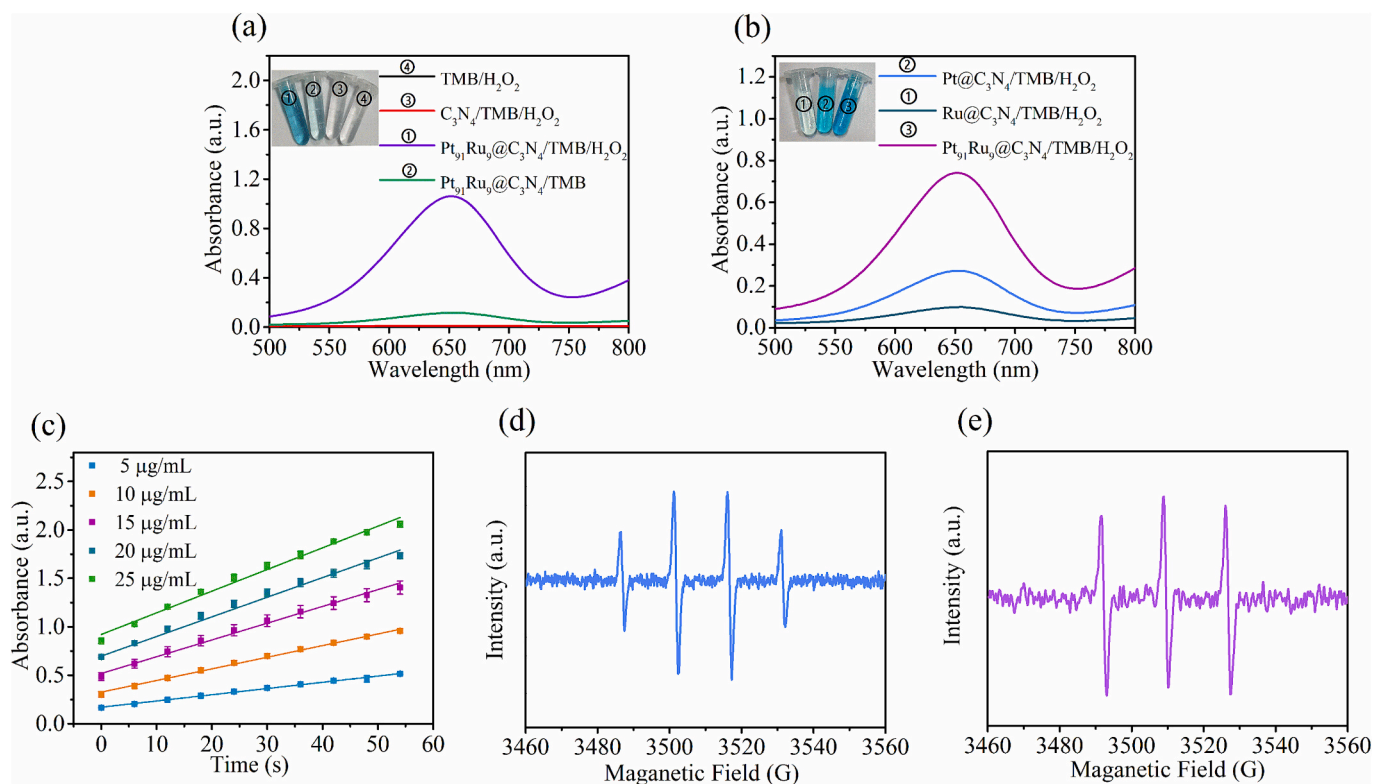

Fig. 3. (a) UV–vis spectra in various reaction systems (blue line: Pt@C$_3$N$_4$/TMB/H$_2$O$_2$, green line: Ru@C$_3$N$_4$/TMB/H$_2$O$_2$, fuchsia line: Pt$_{91}$Ru$_9$@C$_3$N$_4$/TMB). (b) UV–vis spectra of TMB/H$_2$O$_2$, C$_3$N$_4$/TMB/H$_2$O$_2$, Pt$_{91}$Ru$_9$@C$_3$N$_4$/TMB, Pt$_{91}$Ru$_9$@C$_3$N$_4$/TMB/H$_2$O$_2$. (c) The time-dependent absorbance curves for varying concentrations of Pt$_{91}$Ru$_9$@C$_3$N$_4$ in the TMB/H$_2$O$_2$ system (Pt$_{91}$Ru$_9$@C$_3$N$_4$ concentration from down to top: 5, 10, 15, 20 and 25 µg mL^{-1}). ESR spectra for trapping (d) ·OH and (e) ^{1}O$_2$ in the DMPO/Pt$_{91}$Ru$_9$@C$_3$N$_4$ aqueous solution and TEMP/Pt$_{91}$Ru$_9$@C$_3$N$_4$ aqueous solution, respectively. (For interpretation of the references to color in this figure legend, the reader is referred to the web version of this article.)

catalytic performance of $Pt_{91}Ru_9@C_3N_4$. The TMB oxidation reactions at varied $Pt_{91}Ru_9@C_3N_4$ contents were determined by recording the time-dependent changes in UV–vis absorbance at 652 nm. As depicted in Fig. 3c, the rate of TMB oxidation increased as a function of the $Pt_{91}Ru_9@C_3N_4$ concentration from 5 to 25 μg mL^{-1}, with a plateau observed at 15 μg mL^{-1}. The catalytic conditions of $Pt_{91}Ru_9@C_3N_4$ were also estimated under variable pH and temperature conditions. In Fig. S5a and b, pH 5 HAc-NaAc buffer and 45 °C were determined as the optimal conditions for the $Pt_{91}Ru_9@C_3N_4$/TMB/ H_2O_2 colorimetric system.

Radical scavenging trials were then conducted to confirm the species of ROS. As shown in Fig. S6a, the absorbance of $Pt_{91}Ru_9@C_3N_4$/TMB/ H_2O_2 remained nearly unchanged upon the addition of sodium azide (NaN_3), while a noticeable decline was observed after the introduction of p-benzoquinone (p-BQ), indicating superoxide radical ($^1O_2$) as the active intermediate in $Pt_{91}Ru_9@C_3N_4$/H_2O_2 (Yang, Bi, et al., 2024; Yang, Yuan, et al., 2024). Terephthalic acid (TA) was then utilized for additional confirmation of the presence of hydroxyl radicals (·OH) (Zhou, Chen, et al., 2022; Zhou, Wang, et al., 2022). As proved by Fig. S6b, the enhanced fluorescence signals affirmed the existence of ·OH in the $Pt_{91}Ru_9@C_3N_4$/H_2O_2 system. Therefore, $Pt_{91}Ru_9@C_3N_4$ contributed to the generation of the radical species of •OH and $^1O_2$. Electron spin resonance (ESR) spectroscopy was conducted to further examine the active substances generated during the reaction. Using 5,5-dimethyl-1-pyrroline N-oxide (DMPO) as the scavenger, EPR detected a significant •OH signal with an intensity ratio of 1:2:2:1 (Wang et al., 2024), as shown in Fig. 3d. Similarly, when 2,2,6,6-tetramethylpiperidine (TEMP) was employed, characteristic peaks of $^1O_2$ were observed with an intensity ratio of 1:1:1 (Fig. 3e). These findings indicated that both •OH and $^1O_2$ participated in the catalytic reaction, which was consistent with the results of free radical scavenging experiments (Fig. S6a and b).

The steady-state kinetic analysis of $Pt_{91}Ru_9@C_3N_4$ was conducted using the double-fitting method (Li, Chen, et al., 2024; Li, Xie, et al., 2024). The calculated kinetic constants K_m and V_{max} of $Pt_{91}Ru_9@C_3N_4$ from Fig. 4a-d were (0.26 mmol L^{-1}, 4.93×10^{-7} mol L^{-1} s^{-1}) for TMB and (1.01 mmol L^{-1}, 7.19×10^{-7} mol L^{-1} s^{-1}) for H_2O_2, respectively. Hence, $Pt_{91}Ru_9@C_3N_4$ exhibited excellent enzymic kinetic properties, comparable to other reported nanozymes (Table S2). Moreover, the absorbance intensity of $Pt_{91}Ru_9@C_3N_4$/TMB gradually increased with H_2O_2 concentration (Fig. 4e) and maintained an excellent linear relationship with xanthine concentration from 1 to 200 μmol L^{-1} (Fig. 4f) (Y = 0.0058[H_2O_2] + 0.18, μmol L^{-1}, R^2 = 0.999). An LOD of 0.39 μmol L^{-1} was obtained, indicating superior sensitivity of $Pt_{91}Ru_9@C_3N_4$ when compared to other catalytic materials (Table S3). The reliable sensing performance of $Pt_{91}Ru_9@C_3N_4$ toward H_2O_2 revealed promising distinctive colorimetric biosensor for the analysis of H_2O_2 and substances capable of generating H_2O_2.

3.3. Colorimetric sensor for xanthine analysis

The robust peroxidase-mimicking activity of $Pt_{91}Ru_9@C_3N_4$ was used to construct a biosensing platform for the analysis of xanthine. The feasibility of the proposed $Pt_{91}Ru_9@C_3N_4$-based colorimetric sensing strategy was then evaluated. As depicted in Fig. 5a, faint color changes and weak absorbance signals were observed using $Pt_{91}Ru_9@C_3N_4$/TMB, $Pt_{91}Ru_9@C_3N_4$/TMB/xanthine, and $Pt_{91}Ru_9@C_3N_4$/TMB/XOD, separately. As expected, the addition of xanthine and XOD into the $Pt_{91}Ru_9@C_3N_4$/TMB system resulted in increased absorbance at 652 nm, confirming feasible $Pt_{91}Ru_9@C_3N_4$-based colorimetric sensor for the determination of xanthine.

Before xanthine analysis, the reaction conditions of xanthine were optimized to promote the sensitivity of the proposed method, and 0.40 U L^{-1} XOD was selected for xanthine analysis (Fig. S7). Under pH 8 and 37 °C (Wang et al., 2022), the absorbance signal of $Pt_{91}Ru_9@C_3N_4$/ TMB/XOD rose as a function of xanthine content (0–300 μmol L^{-1}) (Fig. 5b). The absorbance signal showed a correlation with the xanthine content with satisfactory linearity from 0.05 to 150 μmol L^{-1} (Y = 0.0024[xanthine] + 0.34, μmol L^{-1}, R^2 = 0.991, inset in Fig. 5b) and a LOD of 8.92 nmol L^{-1} (Fig. 5c). In addition, results of xanthine analysis
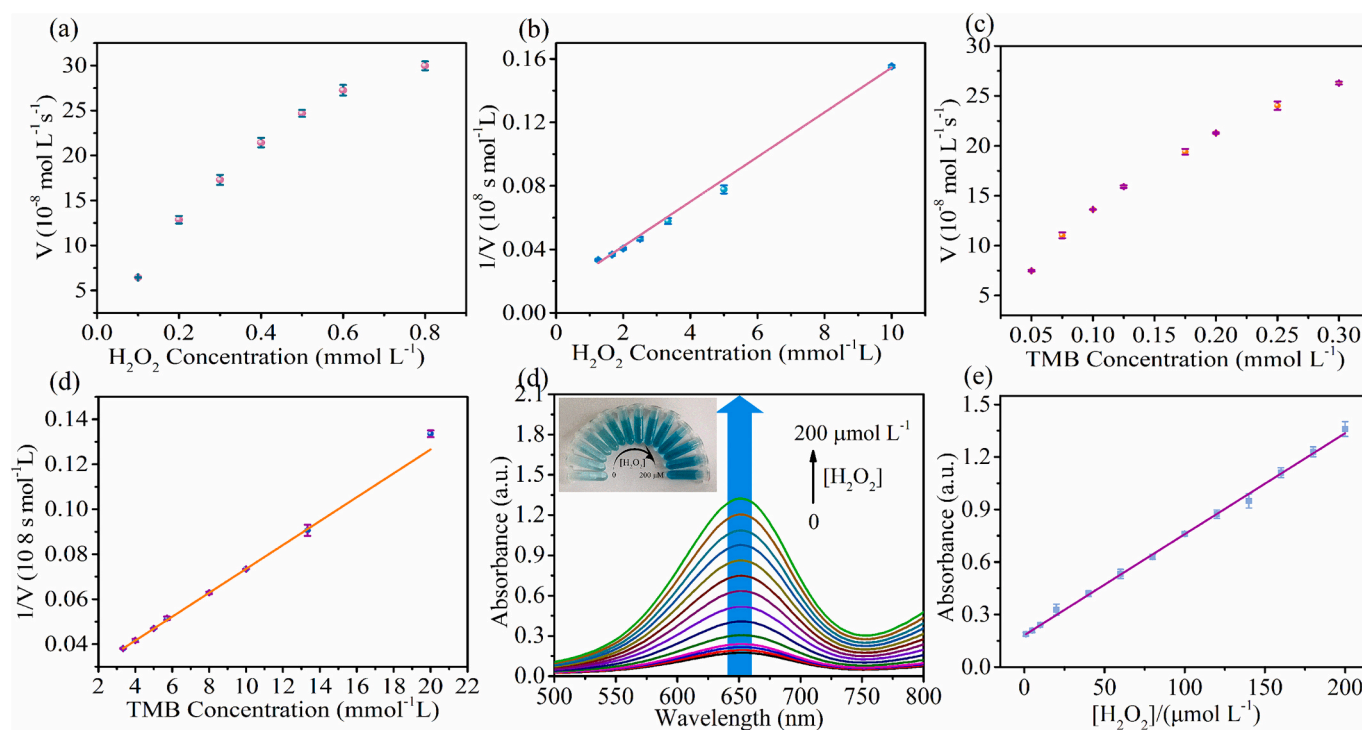

Fig. 4. (a) The influence curves of the H_2O_2 (d, e) and TMB (f, g) concentrations on the catalytic rate of peroxidase, respectively. (h) UV–vis spectra of $Pt_{91}Ru_9@C_3N_4$/TMB following addition of varied contents of H_2O_2. Inset: corresponding snapshots of the test solution. (i) Linear calibration plot of absorption values with varied contents of H_2O_2.
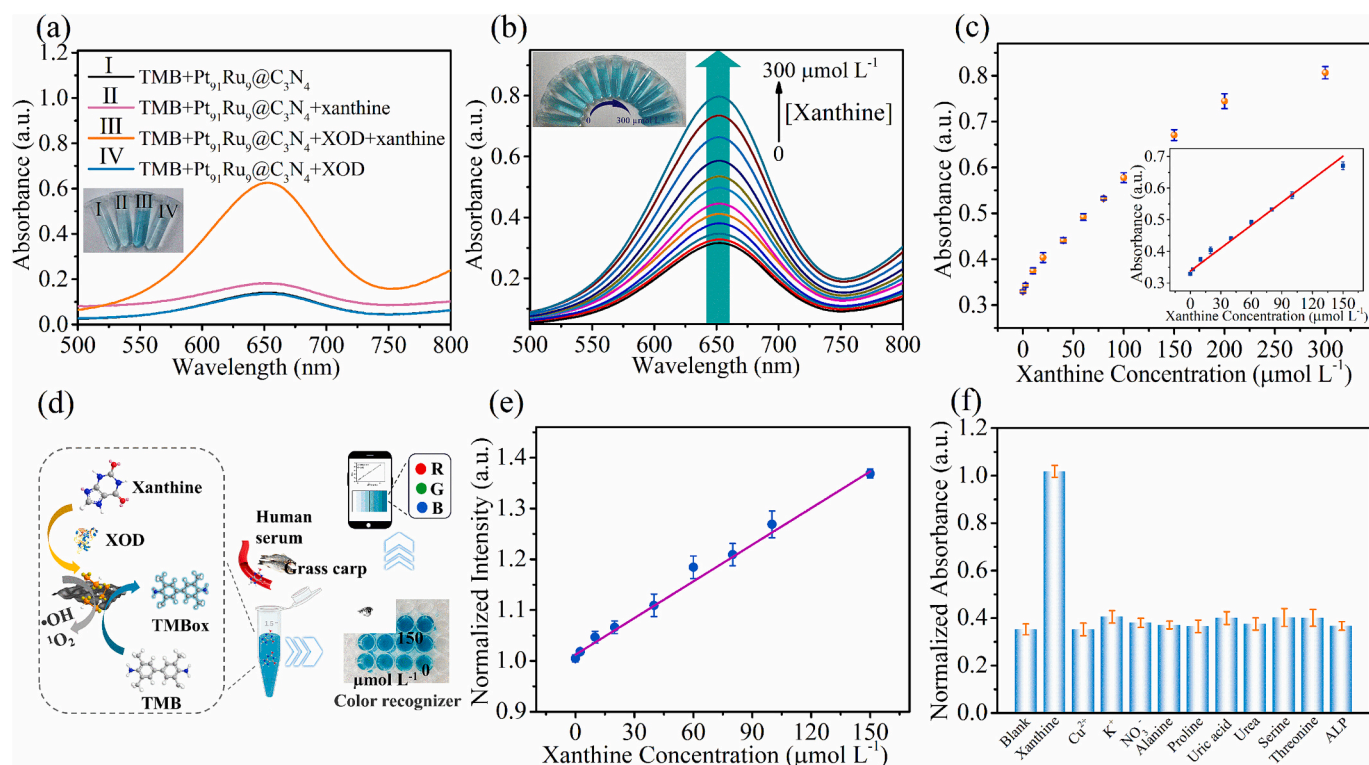
Fig. 5. (a) UV–vis spectra of $Pt_{91}Ru_9@C_3N_4$/TMB, $Pt_{91}Ru_9@C_3N_4$/TMB/xanthine, $Pt_{91}Ru_9@C_3N_4$/TMB/XOD and $Pt_{91}Ru_9@C_3N_4$/TMB/XOD/xanthine (Inset: corresponding color changes). (b) UV–vis spectra of $Pt_{91}Ru_9@C_3N_4$/TMB/XOD following addition of varied contents of xanthine. Inset: corresponding snapshots of the test solution. (c) Linear calibration plot of absorption values with varied contents of xanthine. (d) The $Pt_{91}Ru_9@C_3N_4$/TMB/XOD-based sensing platform based on a smartphone for xanthine analysis and corresponding images of the colorimetric system toward varied xanthine concentrations. (f) Selectivity investigation of the $Pt_{91}Ru_9@C_3N_4$-based colorimetric probe for xanthine analysis. [Alanine] = [Proline] = [Serine] = [Threonine] = [Uric acid] = [Urea] = 1.20 mmol L^{-1}; [ALP] = 20 µg mL^{-1}; [Xanthine] = 0.20 mmol L^{-1}; [Cu^{2+}] = [K^+] = [NO_3^-] = 1 mmol L^{-1}.

compared well with previously reported methods for xanthine measurement (Table S4), verifying the usefulness of $Pt_{91}Ru_9@C_3N_4$/TMB/XOD-based colorimetric sensor for xanthine analysis.

Based on the above colorimetric sensing strategy, a proof-of-concept smartphone-assisted analysis was developed. As illustrated in Fig. 5d, the color gradient changed from light blue to deep blue as the xanthine concentration increased. A linear correlation was observed from 0.05 to 150 µmol L^{-1} between RGB values and xanthine concentration, with $I = 0.0024$[xanthine] + 1.01 (µmol L^{-1}, $R^2 = 0.997$), and a LOD of 17.51 nmol L^{-1} (Fig. 5e). Thus, the smartphone-readout analysis provided a visual and equipment-free ease-operating on-site quantitative analysis of xanthine.

3.4. Selectivity and spiked sample analysis

Selectivity is crucial for evaluating sensor performance. Thus, the absorbance signals of $Pt_{91}Ru_9@C_3N_4$/TMB/XOD system toward various interference substances were investigated and the results are compared in Fig. 5f. Obviously, the influence of alanine, proline, serine, threonine, uric acid, urea, ALP and common ions (Cu^{2+}, K^+, and NO_3^-) on the absorbance intensity of $Pt_{91}Ru_9@C_3N_4$/TMB/XOD can be disregarded, while xanthine showed significantly enhanced absorbance intensity. These results confirmed the satisfactory selectivity of the $Pt_{91}Ru_9@C_3N_4$-based colorimetric probe for xanthine determination.

The practicality of the $Pt_{91}Ru_9@C_3N_4$-based sensor for colorimetric analysis of xanthine was accessed through spiked recovery experiments. The detailed analysis data of serum and grass carp samples exhibited recoveries between 93.95% and 116.50%, with relative standard deviations of less than 3.78% (Table S5 and Table S6), indicating the suitability of $Pt_{91}Ru_9@C_3N_4$-based colorimetric sensor for analysis of xanthine with reliable performance in real samples. Further, a reported

analytical standard method was employed for xanthine determination and compared with our colorimetric sensor. In the sensing strategy (Zhang et al., 2022), Fe/N-CDs was employed as a fluorescence indicator and catalyst for the oxidation reaction between OPD and H_2O_2. And a fluorescence/colorimetric dual-mode sensing platform was developed for xanthine analysis based on the FRET between the oxidation product of oxOPD and Fe/N-CDs. As shown in Fig. S8, the results of xanthine analysis using the $Pt_{91}Ru_9@C_3N_4$-based colorimetric sensor were very close to the values obtained with the Fe/N-CDs-based method (Table S5 and 6), indicating the satisfactory accuracy and reliability of the $Pt_{91}Ru_9@C_3N_4$-based method.

4. Conclusions

In summary, the $Pt_{91}Ru_9@C_3N_4$ with satisfactory catalytic performance was successfully synthesized through a room-temperature co-reduction strategy. By combining the peroxidase-mimicking activity of $Pt_{91}Ru_9@C_3N_4$ and the xanthine/XOD enzyme catalytic system, an efficient, sensitive, and reliable nanozyme-enzyme tandem platform was designed for xanthine analysis. With the assistance of a smartphone app, the $Pt_{91}Ru_9@C_3N_4$/TMB/XOD-based colorimetric sensor achieved convenient and quantitative visual analysis of xanthine without using sophisticated instruments. The proposed colorimetric sensor had been successfully utilized for xanthine analysis in grass carp and serum samples. Overall, a new synthetic approach for the rational design of bimetallic and lamellar nanozymes with efficient catalytical performance was proposed along with insights into the construction of enzyme-nanozyme cascade sensors with high response to target analytes.

CRediT authorship contribution statement

Mengjun Wang: Supervision, Funding acquisition, Conceptualization. **Minghang Jiang:** Data curation. **Xiaojun Luo:** Formal analysis. **Liyun Zhang:** Methodology. **Yi He:** Methodology, Investigation. **Fanjie Xue:** Software, Resources. **Xingguang Su:** Supervision, Funding acquisition.

Declaration of competing interest

The authors declare that they have no known competing financial interests or personal relationships that could have appeared to influence the work reported in this paper.

Data availability

Data will be made available on request.

Appendix A. Supplementary data

Supplementary data to this article can be found online at https://doi.org/10.1016/j.fochx.2024.101588.

References

An, X., Tan, Q., Pan, S., Zhen, S., Hu, Y., & Hu, X. (2022). Determination of xanthine using a ratiometric fluorescence probe based on boron-doped carbon quantum dots and gold nanoclusters. *Microchimica Acta, 189*, Article 148.

Chai, H., Li, Y., Yu, K., Yuan, Z., Guan, J., Tan, W., … Zhang, G. (2023). Two-site enhanced porphyrinic metal-organic framework nanozymes and nano−/bioenzyme confined catalysis for colorimetric/chemiluminescent dual-mode visual biosensing. *Analytical Chemistry, 95*(44), 16383–16391.

Chen, Y., Tang, K., Zhou, Q., Wang, X., Wang, R., & Zhang, Z. (2023). Integrating intelligent logic gate dual-nanozyme cascade fluorescence capillary imprinted sensors for ultrasensitive simultaneous detection of 2,4-dichlorophenoxyacetic acid and 2,4-dichlorophenol. *Analytical Chemistry, 95*(49), 18139–18148.

Dervisevic, M., Custiuc, E., Çevik, E., & Şenel, M. (2015). Construction of novel xanthine biosensor by using polymeric mediator/MWCNT nanocomposite layer for fish freshness detection. *Food Chemistry, 181*, 277–283.

Geng, L., Sun, X., Wang, L., Liu, F., Hu, S., Zhao, S., & Ye, F. (2024). Analyte-induced laccase-mimicking activity inhibition and conductivity enhancement of electroactive nanozymes for ratiometric electrochemical detection of thiram. *Journal of Hazardous Materials, 463*, Article 132936.

Guan, Y., Lu, Y., Zhao, J., Huang, W., & Liu, Y. (2023). Cobalt-based zeolitic imidazole framework incorporated with well-dispersed bimetallic nanoparticles/ions as a multifunctional nanozyme for the degradation of environmental pollutants and discrimination of various phenolic substances. *Chemical Engineering Journal, 465*, Article 142703.

Jesny, S., & Girish Kumar, K. (2017). Non-enzymatic electrochemical sensor for the simultaneous determination of xanthine, its methyl derivatives theophylline and caffeine as well as its metabolite uric acid. *Electroanalysis, 29*(7), 1828–1837.

Jiang, M., Tao, A., Hu, Y., Wang, L., Zhang, K., Song, X., Yan, W., Tie, Z., & Jin, Z. (2022). Crystalline modulation engineering of Ru nanoclusters for boosting ammonia electrosynthesis from dinitrogen or nitrate. *ACS Applied Materials & Interfaces, 14*(15), 17470–17478.

Jiang, X., Liu, W., Li, Y., Zhu, W., Liu, H., Wen, Y., Bai, R., Luo, X., Zhang, G., & Zhao, Y. (2024). WO₃ nanosheets with peroxidase-like activity and carbon dots based ratiometric fluorescent strategy for xanthine oxidase activity sensing and inhibitor screening. *Talanta, 267*, Article 125129.

Li, M., Xie, Y., Zhang, J., & Su, X. (2024). Self-assembled integrated nanozyme cascade biosensor with dual catalytic activity for portable urease analysis. *Analytical Chemistry, 96*(3), 1284–1292.

Li, S., Chen, Z., Liu, M., Yang, F., Zhang, S., Qiao, C., … Yue, W. (2024). Ultrasmall Cu₂O@His with laccase- and catechol oxidase-like activity: Applications in phenolic drug identification and degradation. *Chemical Engineering Journal, 485*, Article 150058.

Li, X., Qian, C., Tian, Y., Yao, N., Duan, Y., & Huang, Z. (2023). Pt-Ru bimetallic nanoclusters with super peroxidase-like activity for ultra-sensitive lateral flow immunoassay. *Chemical Engineering Journal, 457*, Article 141324.

Liu, C., Yan, Y., Zhang, X., Mao, Y., Ren, X., Hu, C., He, W., & Yin, J.-J. (2020). Regulating the pro- and anti-oxidant capabilities of bimetallic nanozymes for the

detection of Fe²⁺ and protection of Monascus pigments. *Nanoscale, 12*(5), 3068–3075.

Lu, Q., Wang, J., Li, B., Weng, C., Li, X., Yang, W., Yan, X., Hong, J., Zhu, W., & Zhou, X. (2020). Dual-emission reverse change ratio photoluminescence sensor based on a probe of nitrogen-doped Ti₃C₂ quantum dots@DAP to detect H₂O₂ and xanthine. *Analytical Chemistry, 92*(11), 7770–7777.

Lyu, L., Hu, X., Lee, S., Fan, M., Kim, G., Zhang, J., … Kang, Y.-M. (2024). Oxygen reduction kinetics of Fe–N–C single atom catalysts boosted by pyridinic N vacancy for temperature-adaptive Zn–Air batteries. *Journal of the American Chemical Society, 146*(7), 4803–4813.

Park, Y., Gupta, P. K., Tran, V. K., Son, S. E., Hur, W., Lee, H. B., … Seong, G. H. (2021). PVP-stabilized PtRu nanozymes with peroxidase-like activity and its application for colorimetric and fluorometric glucose detection. *Colloids and Surfaces. B, Biointerfaces, 204*, Article 111783.

Qiao, W., He, B., Yang, J., Ren, W., Zhao, R., Zhang, Y., Bai, C., Suo, Z., Xu, Y., Wei, M., & Jin, H. (2023). Pt@AuNF nanozyme and horseradish peroxidase-based lateral flow immunoassay dual enzymes signal amplification strategy for sensitive detection of zearalenone. *International Journal of Biological Macromolecules, 254*, Article 127746.

Shen, Y., Gao, X., Chen, H., Wei, Y., Yang, H., & Gu, Y. (2023). Ultrathin C₃N₄ nanosheets-based oxidase-like 2D fluorescence nanozyme for dual-mode detection of organophosphorus pesticides. *Journal of Hazardous Materials, 451*, Article 131171.

Song, P., Wang, M., Xue, Y., Wang, A.-J., Mei, L.-P., & Feng, J.-J. (2022). Bimetallic PtNi nanozyme-driven dual-amplified photoelectrochemical aptasensor for ultrasensitive detection of sulfamethazine based on Z-scheme heterostructured Co₉S₈@In-CdS nanotubes. *Sensors and Actuators B: Chemical, 371*, Article 132519.

Song, Y., Huang, C., & Li, Y. (2023). Nanozyme rich in oxygen vacancies derived from Mn-based metal–organic gel for the determination of alkaline phosphatase. *Inorganic Chemistry, 62*(32), 12697–12707.

Tripathi, A., Elias, A. L., Jemere, A. B., & Harris, K. D. (2022). Amperometric determination of xanthine using nanostructured NiO electrodes loaded with xanthine oxidase. *ACS Food Science & Technology, 2*(8), 1307–1317.

Wang, D., Zhang, L., Wang, C., Cheng, Z., Zheng, W., Xu, P., Chen, Q., & Zhao, Y. (2023). Missing-linker-confined single-atomic Pt nanozymes for enzymatic theranostics of tumor. *Angewandte Chemie International Edition, 62*(19), Article e202217995.

Wang, L., Hong, Y., Liu, E., Wang, Z., Chen, J., Yang, S., Wang, J., Lin, X., & Shi, J. (2020). Rapid polymerization synthesizing high-crystalline g-C₃N₄ towards boosting solar photocatalytic H₂ generation. *International Journal of Hydrogen Energy, 45*(11), 6425–6436.

Wang, L., Sun, M., Zhu, S., Zhang, M., Ma, Y., Xie, D., Li, S., Mominou, N., & Jing, C. (2021). Cu-Ni bimetallic single atoms supported on TiO₂@NG core-shell material for the removal of dibenzothiophene under visible light. *Separation and Purification Technology, 279*, Article 119646.

Wang, M., Zhang, J., Zhou, X., Sun, H., & Su, X. (2022). Fluorescence sensing strategy for xanthine assay based on gold nanoclusters and nanozyme. *Sensors and Actuators B: Chemical, 358*, Article 131488.

Wang, X., Liu, T., Chen, M., Liang, Q., Jiang, J., Chen, L., Fan, K., Zhang, J., & Gao, L. (2024). An erythrocyte-templated iron single-atom nanozyme for wound healing. *Advanced Science, 11*(6), Article 2307844.

Wu, J., Wang, X., Wang, Q., Lou, Z., Li, S., Zhu, Y., … Wei, H. (2019). Nanomaterials with enzyme-like characteristics (nanozymes): Next-generation artificial enzymes (II). *Chemical Society Reviews, 48*(4), 1004–1076.

Xu, N., Xiao, M., Yu, Z., Jin, B., Yang, M., & Yi, C. (2024). On-site quantitation of xanthine in fish and serum using a smartphone-based spectrophotometer integrated with a dual-readout nanosensing assay. *Food Chemistry, 431*, Article 137107.

Yang, D., Yuan, M., Huang, J., Xiang, X., Pang, H., Wei, Q., Luo, X., Cheng, C., Qiu, L., & Ma, L. (2024). Conjugated network supporting highly surface-exposed Ru site-based artificial antioxidase for efficiently modulating microenvironment and alleviating solar dermatitis. *ACS Nano, 18*(4), 3424–3437.

Yang, X., Bi, Z., Yin, C., Zhang, S., Song, D., Huang, H., & Li, Y. (2024). A colorimetric sensor array based on peroxidase activity nanozyme for the highly efficient differential sensing of tea polyphenols and Tieguanyin adulteration. *Food Chemistry, 432*, Article 137265.

Zhang, F., Wang, M., Zeng, D., Zhang, H., Li, Y., & Su, X. (2019). A molybdenum disulfide quantum dots-based ratiometric fluorescence strategy for sensitive detection of epinephrine and ascorbic acid. *Analytica Chimica Acta, 1089*, 123–130.

Zhang, L., Li, Q., Jia, S., Huang, Z., & Luo, Y. (2018). Effect of different stunning methods on antioxidant status, in vivo myofibrillar protein oxidation, and the susceptibility to oxidation of silver carp (*Hypophthalmichthys molitrix*) fillets during 72 h postmortem. *Food Chemistry, 246*, 121–128.

Zhang, W., Wu, Y., Liu, X., Liu, Y., Zhang, Y., Wang, W., Mu, X., Su, R., Sun, Y., Song, D., & Wang, X. (2022). A universal sensing platform based on iron and nitrogen co-doped carbon dots for detecting hydrogen peroxide and related metabolites in human fluid by ratiometric fluorometry and colorimetry. *Spectrochimica Acta Part A: Molecular and Biomolecular Spectroscopy, 272*, Article 121003.

Zhang, X., Yang, Q., Lang, Y., Jiang, X., & Wu, P. (2020). Rationale of 3,3′,5,5′-tetramethylbenzidine as the chromogenic substrate in colorimetric analysis. *Analytical Chemistry, 92*(18), 12400–12406.

Zhou, C., Chen, J., Wang, G., & Su, X. (2022). Heparin-enhanced peroxidase-like activity of iron-cobalt oxide nanosheets for sensitive colorimetric detection of trypsin. *Microchimica Acta, 189*(4), 135.

Zhou, X., Wang, M., Chen, J., & Su, X. (2022). Cascade reaction biosensor based on Cu/N co-doped two-dimensional carbon-based nanozyme for the detection of lactose and β-galactosidase. *Talanta, 245*, Article 123451.

Zou, X., Huang, L., Liu, Y., Chen, Q., Zheng, X., Fan, M., & Gong, Z. (2023). Metal-organic framework-derived Fe/C/Bi₂O₃ as peroxidase-like nanozymes for the detection of organophosphorus pesticides. *Sensors and Actuators B: Chemical, 393*, Article 134121.